Journal of Colloid and Interface Science 582 (2021) 669–677

Contents lists available at ScienceDirect

Journal of Colloid and Interface Science

journal homepage: www.elsevier.com/locate/jcis

The intriguing role of rhamnolipids on plasma membrane remodelling: From lipid rafts to membrane budding

Benedetta Come [a], Maressa Donato [b,c], Lucia Francesca Potenza [a], Paolo Mariani [a], Rosangela Itri [b,*], Francesco Spinozzi [a,**]

[a] Department of Life and Environmental Sciences, Polytechnic University of Marche, Italy
[b] Institute of Physics, University of São Paulo, Brazil
[c] Center for Laser and Applications, Nuclear and Energy Research Institute, São Paulo, Brazil

GRAPHICAL ABSTRACT

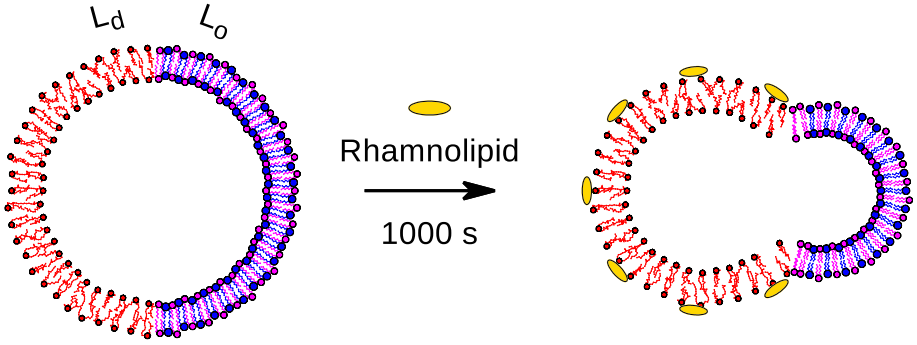

ARTICLE INFO

Article history:
Received 29 May 2020
Revised 24 July 2020
Accepted 6 August 2020
Available online 17 August 2020

Keywords:
Membrane remodeling
Lipid rafts
Giant unilamellar vesicles
Rhamnolipid
Biosurfactant
Membrane budding
Endocytosis

ABSTRACT

Rhamnolipids (RLs) comprise a class of glycolipids produced by *Pseudomonas aeruginosa* under appropriate culture medium. They act as biosurfactants being composed by a hydrophilic head of either one (mono-RL) or two (di-RL) rhamnose moieties coupled to hydroxyaliphatic chains. It is well accepted that RLs present low biolitic activity as compared to other synthetic surfactants. However, their mechanisms of action in biological systems are not well defined yet. The interaction of RLs with lipid bilayers are here investigated to address how they impact on plasma membrane at molecular level. Our experimental approach was based on a deep analysis of optical microscopy data from giant unilamellar vesicles (GUVs) dispersed in aqueous solutions containing up to 0.5 mM of commercially available RLs (a mixture of mono-RL, 33–37 mol%, and di-RL, 63–67 mol%, *cmc* of 0.068 ± 0.005 mM). GUVs were made up of a single lipid POPC and a ternary system containing DOPC, sphingomyelin and cholesterol, which mimic lipid raft platforms. Our results demonstrate that RLs have a low partition in the lipid bilayer in respect to the total molecules in solution. We suppose that RLs insert in the outer leaflet with low propensity to flip-flop. In the case of POPC GUVs, the insertion of RL molecules in the outer leaflet impairs changes in spontaneous membrane curvature with incubation time. Then, small buds are formed that remain linked to the original membrane. No changes in membrane permeability have been detected. A remarkable result refers to the insertion of RLs in membranes containing liquid ordered (L_o) - liquid disordered (L_d) phase coexistence. The rate of interaction has been observed to be higher for L_d phase than for L_o phase ($0.12 \cdot 10^{-6}$ s^{-1} and $0.023 \cdot 10^{-6}$ s^{-1} for L_d and L_o, respectively, at RL concentration of 0.5 mM). As a consequence, the preferential RL insertion in L_d phase may also alter the membrane spontaneous

* Corresponding author.
** Corresponding author.
E-mail addresses: itri@if.usp.br (R. Itri), f.spinozzi@univpm.it (F. Spinozzi).

https://doi.org/10.1016/j.jcis.2020.08.027

curvature which, coupled to the change in the line tension associated to the domains boundary, conducted to L_o domain protrusion. Even if it has been observed on a model system, such membrane remodelling might correlate to endocytic processes activated in cell membranes, regardless of the participation of specific proteins. Further, changes imposed by RLs in lipid rafts may affect the association of key proteins enrolled in cell signaling, which may perturb cell homeostasis.

1. Introduction

It is well recognized that one of the biggest problems in the industrialized world is the contamination with dangerous and toxic chemicals of soil, sediments, groundwater, surface water and air [1–3]. The search of new environmental technologies includes bioremediation, which envisages the correct use of either microorganisms or microbial processes to biodegrade contaminants [4,5]. On this ground, an increasing interest in a new class of surfactants, referred to as biosurfactants, has taken place over the last two decades. They are naturally produced by many organisms, especially by bacteria [6,7]. Among the most investigated and exploited biosurfactants there are the glycolipids, which are carbohydrates with aliphatic or hydroxyaliphatic chains. In particular, amid glycolipids a relevant role is played by rhamnolipids (RLs), mainly produced by *Pseudomonas aeruginosa*, composed by a hydrophilic head constituted of either one (mono-RL) or two (di-RL) rhamnose moieties and one or two tails of β-hydroxydecanoic acids (Fig. 1), linked to a large variety of 3-(hydroxyalkanoyloxy) alkanoic acids carbon chain. Like other synthetic surfactants, RLs are able to reduce the water surface tension significantly [8–10] and to form emulsions [11]. Further, they have been successfully applied on bioremediation processes with the aim of either degrading organic waste or reducing its concentration down to the limits imposed by regulatory authorities [12]. Of note, concerning bioremediation activities in oil-contaminated waters, it has been reported that RLs can recover up to 98% of crude oil from the refractory waste, both on a laboratory scale and on pilot plants [13]. They are also effective in washing up to 95% of synthetic oil from sand [14]. RLs have been also applied in pharmaceutics, cosmetics, agriculture and other industrial sectors. For instance, we have previously demonstrated that RLs can be used as epithelial permeability enhancer [8]. Besides, antiviral, antimycotic, mycoplasmacidal, algicidal and zoosporcidal activities have been reported [15,16]. Due to the approval of the United States Environmental Protection Agency (EPA), RLs have been applied to horticultural and agricultural crops as effective biofungicides [17].

In spite of potential RLs applications, very little is known about the molecular basis of some biological actions of these biosurfactants. For instance, permeabilization and/or membrane rupture are important for biocide action. On the other hand, for human consumption and environmental purposes, it is quite important to correlate the RLs action mechanisms on biological membranes with their molecular structures, which confer their amphipathic properties. It is known that the critical micellar concentration (*cmc*) of pure RLs, which form micelles of *circa* 20–30 nm in size, and their mixtures is dependent on their chemical composition [18,19]. However, few studies have been dedicated to explore the interaction between RLs, below and above *cmc*, and biological interfaces at molecular level. In this regard, Ortiz and coworkers investigated the effects of di-RL, which behaves as an inverted-cone shaped molecule [20,9], on the structural properties of phosphatidylcholine (PC) model membranes by differential scanning calorimetry, X-ray diffraction, fluorescence and infrared spectroscopies [21,22]. The combined results revealed that di-RL intercalates in the PC bilayers promoting an increase in phospholipid hydrocarbon chain disorder. This process perturbs the packing of PC molecules emphasized by the reduction of cooperativity in the gel to liquid crystalline phase transition. Further, di-RL induces leakage of carboxifluorescein (CF) entrapped into POPC unilamellar vesicles [23]. Interestingly, the presence of a lag period was evident for all di-RL concentrations below *cmc* of 0.11 mM, being shorter for increasing di-RL concentration. Such CF leakage was not accompanied by membrane disruption. On the contrary, at di-RL concentrations above *cmc*, POPC bilayer displays a quick CF-leakage concomitantly with membrane solubilization. Of note, the presence of phosphatidylethalonamine, a cone-shaped lipid, inhibits the effect of di-RL in POPC membranes due to favoured lipid packing [20,23]. In addition, cholesterol exhibits a protective action against membrane permeabilization [23]. Such findings could be of particular interest because plasma membrane of eukaryotic cells can contain up to 50 mol% of cholesterol, which would protect the human cells from di-RL damage in a first insight.

Interestingly, Ortiz and coworkers [23] also investigated the impact of di-RL on red blood cells used as model cells. The authors have demonstrated that di-RLs at concentrations below *cmc* are able to promote human erythrocytes permeabilization via detergent-like mechanism. In parallel, electron microscopy images have revealed alterations of red blood cell morphology from usual biconcave disk-like shape to swollen cells (spherocytes), some of them presenting protrusions on cell surface (echinocytes). Such morphological changes must indicate either a di-RL preferential partition into the outer plasma membrane or alterations in the cytoskeleton [23]. Of note, a small lag period has been observed

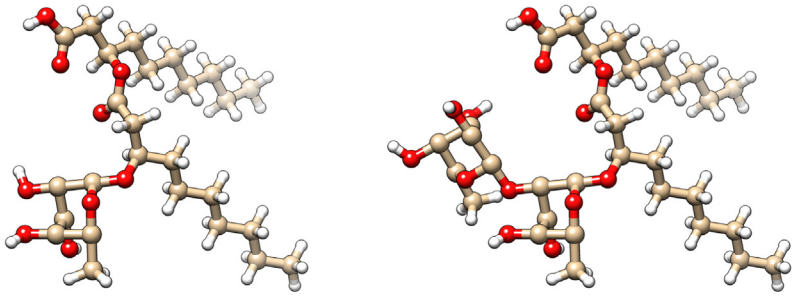

Fig. 1. Ball-and-stick representations of a mono-RL (RL – C_{10} – C_{10}, left) and a di-RL (RL – RL – C_{10} – C_{10},right).

for all studied di-RL concentrations below *cmc*, indicating that an initial di-RL interaction mechanism upon the cells takes place prior to erythrocytes hemolysis. Such mechanism of interaction remains yet obscure in the literature.

Regarding *in vivo* assays, the impact of RL against a phagotropic alga *Ochromonas danica* has been recently reported [24]. Interestingly, such alga species represents a group of phagotropic flagelletes ecologically important for aquatic systems, with no protective cell wall. In this case, biolitic and permeability effects on the algal plasma membrane are only observed at RL concentrations above *cmc*, unlike the impact of synthetic surfactants as sodium dodecyl sulfate (SDS) that occurs at sub-micellar concentrations. It means that whereas individual SDS molecules are able to damage *O.danica* cell membrane probably forming mixed micelles with membrane lipids, RLs must preferentially interact with the plasma membrane just when micelles are formed in solution. Also, RL-induced motility loss was identified [24].

Therefore, although several preceding works have addressed the influence of the biosurfactant RL on biomembranes, its mechanism of action on plasma membrane at molecular level remains elusive. It should bear in mind that plasma membrane lipid composition is close to a critical point of phase separation [25]. From the biological point of view, being close to a critical point the cell requires much less energy to promote lipid demixing and to create lipid heterogeneity known as lipid rafts. Such rafts platforms mediate protein-protein and protein-membrane interactions that are the key actors in cell signalling processes [25–28]. In this light, here we investigate the effect of a commercially available RL mixture composed of mono-RL (33–37 mol%) and di-RL (63–67 mol%) [8] on plasma membrane models represented by giant unilamellar vesicles (GUVs) above *cmc*. Two types of GUVs were challenged by the RL mixture for comparison purposes and observed under an optical microscopy in both phase contrast and fluorescence modes. They were: GUVs made up of a single lipid, POPC, and of a ternary mixture of DOPC, sphingomyelin (SM) and cholesterol (CHOL), at molar ratio 1:1:1, which present liquid-ordered (L_o) liquid-disordered (L_d) phase coexistence [29] resembling lipid rafts [29]. In this way, changes in lipid rafts organization, membrane remodelling, permeabilization and membrane disruption elicited by RLs can be simultaneously evaluated by optical microscopy. Such experimental procedure allows us to describe the RLs action mechanisms underlining the plasma membrane response, as follows.

2. Materials and methods

2.1. Sample preparation

RL from *Pseudomonas Aeruginosa* (powder, 90% purity) was purchased from Sigma-Aldrich (Poole, UK). As described by Perinelli et al. [8], this commercial product is mainly composed by a mixture of mono-rhamnolipids (33–37 mol%) and di-rhamnolipids (63–67 mol%) and the *cmc* in water was estimated as 0.16 mM.

Herein, RL will be dispersed in glucose solution as described below. Accordingly, *cmc* was determined by surface tension and amounted to 0.068 ± 0.005 mM (Fig. S1).

All studied lipids were acquired from Sigma-Aldrich: POPC (2-oleoyl-1-palmitoyl-*sn*-glycero-3-phosphocholine), DOPC (1,2-di (cis-9-octadecenoyl)-*sn*-glycero-3-phosphocholine), sphingomyelin (SM, N-acyl-4-sphingenyl-1-O-phosphorylcholine, N-Acyl-D-sphingosine-1-phosphocholine), cholesterol (CHOL, 3β-hydroxy-5-cholestene, 5-cholesten-3β-ol) and DOPE (1,2-dioleoyl-*sn*-glycero-3-phosphoethanolamine)-rhodamine, Rho-PE. All other chemicals and solvents were purchased from Sigma Aldrich (Saint Louis, MO) and used without further purification.

GUVs were prepared by the electroformation procedure using POPC, POPC/Rho-PE (0.1 mol%) and DOPC, SM, CHOL (molar ratio 1:1:1) containing Rho-PE (0.1 mol%). Briefly, 20 μL of 1.0 g/L total lipid in chloroform solution were spread on the surfaces of two conductive glass slides coated with indium tin oxide (ITO slides, Sigma-Aldrich, Saint Louis, MO). The glass slides were placed with their conductive sides facing each other and separated by a 2 mm thick Teflon frame. The chamber was filled with a 0.2 M sucrose solution up to a volume of 1.0 mL. The glass plates were connected to a function generator applying an alternating voltage of 2 V with 10 Hz frequency for 2 h. The electroformation of GUVs composed of DOPC:SM:CHOL was conducted at 55 °C. These GUVs were left at 4 °C overnight and observed in the following day. Subsequently, 100 μL of electroformed GUVs were mixed to 600 μL of a 0.2 M glucose solution containing RL and immediately transferred to the microscope chamber to perform continuous observations. The final total lipid concentration was 0.00286 g/L, whereas the RL concentration ranged from 0.1 mM to 0.5 mM. The osmolarities of the sucrose and glucose solutions were measured with a cryoscopic osmometer Osmomat 030 (Gonotec, Germany) and carefully matched to avoid osmotic pressure effects thus guaranteeing the optical contrast. Experiments were done at least in triplicate.

2.2. Microscope observations

Vesicles were observed in the phase contrast and fluorescence modes by means of an inverted microscope Axiovert 200 (Carl Zeiss, Jena, Germany) equipped with a Plan Neo-Fluar 63X Ph2 objective (NA 0.75). Images were recorded with an AxioCam HSm digital camera (Carl Zeiss). A mercury lamp HBO 103 W, with excitation and emission filters at 540–552 nm and 575–640 nm, respectively, was used in the fluorescence mode. The effect of lipid oxidation was controlled by the use of low intensity illumination in the fluorescence microscopy to avoid artifacts due to light-induced domain formation by the Rho-probe [30,31]. All measurements were done at (23 ± 2) °C.

2.3. Data analysis

Several hundreds of snapshots of the GUVs, collected as a function of time after the mixing with a glucose solution at different RL concentration, were analyzed by using original macros that we have developed under the ImageJ software [32].

GUVs formed by POPC appear approximately as circles when observed with the microscope, indicating that their shape is almost spherical. By a set of user-selected points placed over the border of a POPC GUV microscopy snapshot, a first ImageJ macro allows to calculate the coordinates of the center and the radius R of the best circle passing among the points (see Fig. S2 in the SI), corresponding to the radius of the spherical vesicle, together with their standard deviations. Details are shown in Sec. S2 of the SI.

On the other side, the shape of GUVs constituted by DOPC:SM:CHOL, observed with the microscope as a function of the time after the interaction with RL, appears as a combination of two spherical caps [33], as shown in Fig. 2. To note, we have considered, among the GUVs formed by two spherical caps, only the ones that, during the observation time, appear to maintain the line joining the two spherical caps centers almost parallel to the observation plane. In this cases, in order to estimate the radii of the two spherical caps, R_1 and R_2 (assuming $R_1 \geqslant R_2$), and the distance r_{12} between their centers, together with their standard deviations, a second ImageJ macro has been developed, which requires the user to select two sets of points over the border, respectively, of the two circular arcs that appear in the microscope snapshot. The equations exploited by this ImageJ macro are detailed in Sec. S3 of the SI.

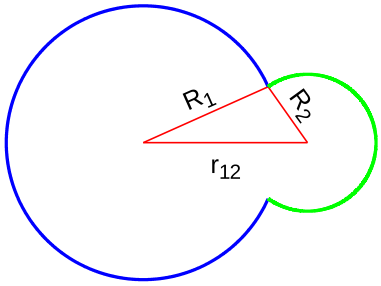

Fig. 2. Projection into the plan of a vesicle formed by sealing a vesicle of radius R_1 with a vesicle of radius R_2, being r_{12} the distance between the centers of the two vesicles. Blue and green arcs refer to A_1 and A_2 surfaces, respectively. (For interpretation of the references to color in this figure legend, the reader is referred to the web version of this article.)

The surfaces of the two spherical caps with radius R_1 and R_2, respectively, are given by the following expressions [33]

$$A_1 = \frac{\pi R_1}{r_{12}}(R_1^2 - R_2^2 + r_{12}(r_{12} + 2R_1)) \quad (1)$$

$$A_2 = \frac{\pi R_2}{r_{12}}(R_2^2 - R_1^2 + r_{12}(r_{12} + 2R_2)) \quad (2)$$

The total surface of the two sealed spherical caps vesicle is clearly $A = A_1 + A_2$, whereas the enclosed volume of the whole vesicle is calculated according to

$$V = \frac{\pi}{12 r_{12}}(R_1 + R_2 + r_{12})^2 (3R_1^2 + 2R_1 r_{12} - r_{12}^2 - 6R_1R_2 + 2r_{12}R_2 + 3R_2^2) \quad (3)$$

Equations exploited to calculate the standard deviations of surface areas (A_1, A_2 and A) and volume V are reported in Sec. S3 of the SI.

3. Results and discussion

In order to investigate the interaction between RLs and mimetic phospholipid plasma membranes, we initially considered homogeneous POPC GUVs exposed to the biosurfactants. Spherical vesicles dispersed in 0.1 mM RL-containing glucose solution (i.e. above *cmc*) do not present any morphological alteration and preserve their optical contrast over approximately 1000 s of continuous observation. It means that, at such concentration, RLs did not cause membrane permeabilization, which would be characterized by sugar exchange between the inner and outer GUVs compartments. Such finding apparently contrasts with those reported by Sánchez et al. [23], where the authors have evidenced 100% of CF release from POPC LUVs interacting with 0.1 mM di-RL (near its *cmc* of 0.11 mM in water) in an elapsed time of 600 s, with no membrane solubilization. It should be remarked, however, that here we investigate POPC GUVs incubated in a solution containing 0.1 mM of a mixture of mono and di-RLs, relatively close to the *cmc* value of 0.068 ± 0.005 mM in glucose solution (Fig. S1.) Further, the GUVs membrane curvature could also hinder the inverted-cone shaped RLs molecules insertion into POPC bilayers in respect to LUVs, thus justifying the differences found in membrane permeabilization data.

Fig. 3 shows typical morphological changes imposed by submitting POPC GUVs to increasing RL concentrations. At 0.2 mM RL (*circa* 3-fold the *cmc*) the membrane suffers only subtle fluctuations with the emission of few small buds (small micro-sized vesicles linked to the original GUV, Fig. 3, panel A), preserving the original membrane surface area over time (Fig. 4, green circles). This was accounted for by evaluating, with the first ImageJ macro (see Sec. "Data analysis"), the radius of a circle surrounding the GUV spherical shape (Fig. 3, panel B).

On the other hand, in the case of POPC bilayers dispersed in 0.5 mM RL containing outer solution, RL promotes marked GUVs fluctuations (Fig. 3, panels C and D) accompanied by significant area increase after *circa* 600 s of membrane:RL contact (maximum at 634 s, Fig. 4, red circles). This indicates that RL molecules inserted in the membrane produce an excess of surface area. As response, the membrane emits buds (highlighted as fluorescent small GUVs linked to the original one, Fig. 3, panel C, fluorescence mode) to release the area excess returning to its original area. In this way, both the lipid bilayer forming the bud and the surrounding membrane matrix are in fluid state. Then, phospholipid molecules can flow and rearrange themselves within the plane of the membranes [34]. Of note, due to RLs bulky molecular structure (Fig. 1) we suggest that they must be mainly located in the outer leaflet of the membrane with no or very slow flip-flop. Interestingly, we calculate the ratio of RL bound to the outer leaflet in respect to the POPC lipid based on the POPC GUV area increase (Fig. 4). This ratio amounted to 0.092 ± 0.004 at maximum area increase (Eq. S32). Further, the time evolution of the fraction of GUV-bound RL in respect to total RL added to the outer solution resulted to be $(4.3 \pm 0.2) \cdot 10^{-6}$ s^{-1} (Eq. S36 with $\zeta_d = 116$). Therefore, the RL partition in POPC is low, even tough it is able to promote increase in membrane area, followed by buds protusion. No changes in membrane permeability have been detected under RL influence, since no optical contrast fade has been observed. So, packing defects, which could lead to observable GUV leakage, were not evidenced in these experiments. Moreover, neither membrane solubilization nor rupture have been registered in the elapsed time of $\approx$ 1000 s, unlike the deleterious effects previously demonstrated by synthetic surfactants as SDS and Triton-X on POPC GUVs [35–38].

In the following, we present the optical microscopy results regarding the impact of RLs on GUVs presenting L_o-L_d phase coexistence. The heterogeneous vesicles were made of equimolar contents of DOPC:SM:CHOL at the concentration 0.00286 g/L (corresponding to 0.00431 mM of total lipids molecules) and 0.1 mol% of Rho-PE. Fig. 5, panels A and C, shows representative GUVs images exposed to 0.2 mM RL and 0.5 mM RL, respectively.

It is well known that L_d-L_o phase coexistence is easily recognized by fluorescence microscopy since the fluorescent probe Rho-PE prefers to partition in L_d phase [29]. In this way, Fig. 5 displays an initial dark liquid ordered L_o domain within a bright liquid disordered L_d phase in a spherical GUV. Interestingly, as time evolves, RL-induced membrane remodeling gradually takes place resulting into L_o phase outward budding. Note that L_o phase protrusion is faster for increasing RL amount. It should be note that experiments in the absence of RL were carried out as control and no alterations in the original GUVs were observed.

Herein we analyse such morphological change by taking into account two circles of radii R_1 (left side) and R_2 (right side) that encompass the GUV (Fig. 2), related to the displacement of L_d phase in respect to the L_o phase, respectively, together with the distance r_{12} between their centres. Best circles and center-to-center distances, obtained through the second ImageJ macro as described in Sec. "Data analysis", are superimposed to the microscope images in Fig. 5, panel B, for 0.2 mM RL and panel D for 0.5 mM RL. Corresponding values of R_1, R_2 and r_{12} are plotted as a function of the time in Fig. 6, panels A and B, whereas the values of the total GUV surface A are displayed in panel C, of the L_d and L_o surfaces A_1 and A_2, calculated with Eqs. 1,2, respectively, in panels D and E, and of GUV volume V in panel F. To note, also the values obtained by the microscope observations of the control DOPC:SM:CHOL GUVs in the absence of RL are shown.

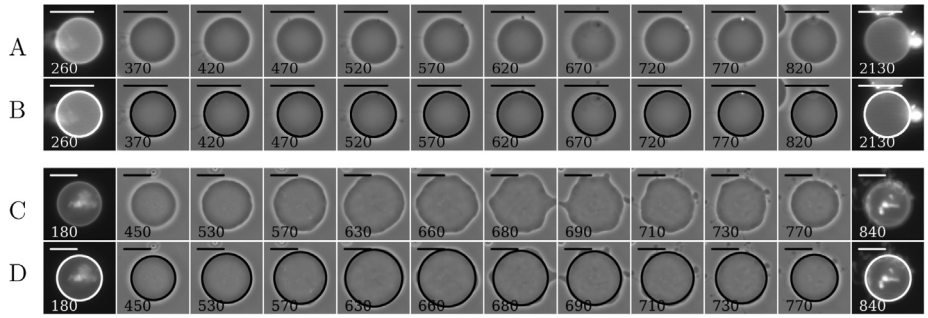

Fig. 3. Representative GUV fluorescence images (the first and last ones of each row) and phase contrast images of POPC (0.00376 mM) with 0.1 mol% Rho-PE dispersed in 0.2 mM RL (panel A) and 0.5 mM RL-containing glucose solution (panel C). The time sequence, expressed in seconds in the bottom left corner of each image, refers to the elapsed time after mixing RL with GUV solution (considered as time 0 s). The images of panels A and C with superimposed the best circle surrounding the GUVs determined with the first ImageJ macro are reported in panels B and D, respectively. The top right bars span 20 μm.

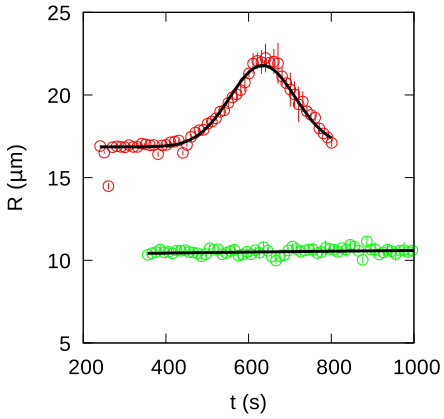

Fig. 4. Time-dependence of the radius of POPC GUV in the presence of 0.2 mM (green circles) and 0.5 mM (red circles) RL. The black line represents the best fit to the data using a Gaussian function over a flat background. Fitting parameters for GUVs interacting with 0.5 mM RL are: background (16.857 ± 0.004) μm, height (4.9 ± 0.3) μm, standard deviation (79 ± 3) s, peak position (634 ± 3) s. (For interpretation of the references to color in this figure legend, the reader is referred to the web version of this article.)

Both the time evolution of circles' radii R_i $(i = 1, 2)$ as well as the distance r_{12} between the centres of the circles have been approximated with the following sigmoidal behaviours,

$$R_i(t) = R_i^0 + (R_i^\infty - R_i^0)\frac{1 - \exp\left(\frac{t}{\Delta t_{R_i}}\right)}{2 - \exp\left(\frac{t}{\Delta t_{R_i}}\right) - \exp\left(\frac{t_{0,R_i}}{\Delta t_{R_i}}\right)} \tag{4}$$

$$r_{12}(t) = r_{12}^\infty \frac{1 - \exp\left(\frac{t}{\Delta t_{r_{12}}}\right)}{2 - \exp\left(\frac{t}{\Delta t_{r_{12}}}\right) - \exp\left(\frac{t_{0,r_{12}}}{\Delta t_{r_{12}}}\right)} \tag{5}$$

where R_i^0 represents the value at the beginning $(t = 0)$, R_i^∞ or r_{12}^∞ are the values at the plateau (when the time t tends to infinity), t_{0,R_i} or $t_{0,r_{12}}$ are the time values in the middle of the transition and Δt_{R_i} or $\Delta t_{r_{12}}$ corresponds to the time widths at the transition.

Fitting parameters obtained by applying those approximations are reported in Table 1. The time trends of the total and the partial GUV surfaces (A, A_1 and A_2), as well as the ones of the GUV volumes V result to be almost linear, as shown by the best fitting straight lines reported in Fig. 6, panels C-F. The corresponding slopes (m_A, m_{A_1}, m_{A_2} and m_V) and intercepts at $t = 0$ ($A_0, A_{1,0}, A_{2,0}$ and V_0) are shown in Table 1.

Results indicate that, for 0.2 mM RL, whereas both radii attributed to the disordered and the ordered phases (R_1 and R_2, respectively) are quite similar and slightly decrease of *circa* 6% over time (Fig. 6, panel A, open and closed circles, respectively, and Table 1), the distance r_{12} between their centres changes of *circa* 6 μm in an elapsed time of 1000 s of RL-heterogeneous GUV contact, with a mid transition time $t_{0,r_{12}} \approx 540$ s (Fig. 6, panel B, circles and Table 1). Such transition is accompanied by a tiny increase in the comprised area (Fig. 6, panel C (circles) and Table 1: the slope is $m_A \approx 0.3$ μm^2 s^{-1}, corresponding to a relative variation from 180 to 1000 s in the order of 4%), while the volume remains almost unaltered (Fig. 6, panel F (triangles) and Table 1. From one hand, the constancy of the volume confirms that during the observation time the line joining the two spherical cap centers remains almost

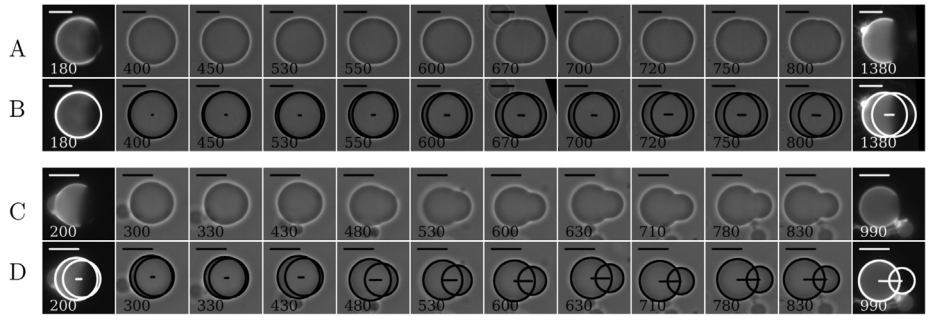

Fig. 5. Representative fluorescence images (the first and last ones of each row) and phase contrast images of a GUV composed by DOPC, SM, CHOL (1:1:1) (at 0.00431 mM total lipid concentration) and 0.1 mol% Rho-PE dispersed in a glucose solution containing 0.2 mM RL (panel A) and 0.5 mM RL (panel C). The time sequence, expressed in seconds in the bottom left corner of each image, refers to the elapsed time after mixing RL with GUV solution (considered as time 0 s). The images of panels A and C with superimposed the best two circles surrounding the GUVs determined with the second ImageJ macro are reported in panels B and D, respectively. All images have been rotated in order to get the line connecting the centres of the two circles (shown in panels B and D) in the horizontal direction, with the large and the small circle, of radius R_1 and R_2, on the left and the right side, respectively (Fig. 2). The distance r_{12} (Eq. 5) between the centres (Fig. 2) is shown as black or a white line. The top right bars span 20 μm.

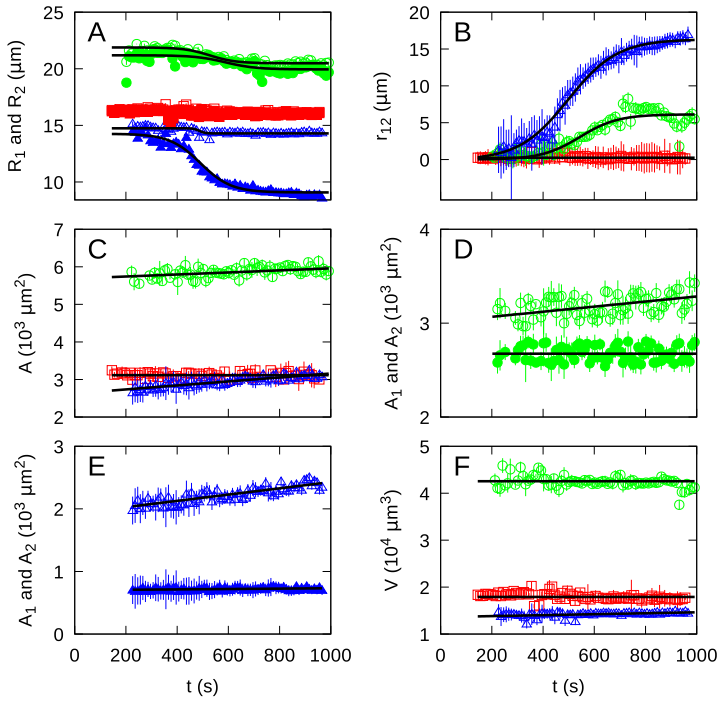

Fig. 6. Time-dependence of the geometrical parameters of the GUVs formed by DOPC, SM, CHOL (1:1:1) in the absence of RL (red squares) and in the presence of 0.20 and 0.50 mM RL (green circles and blue triangles, respectively). Panel A: large (R_1, open symbols) and small (R_2, filled symbols) circle radius and best fitting obtained with sigmoidal function (Eq. 4). Panel B: centre-to-centre distances and best fitting obtained with sigmoidal function (Eq. 5). Panel C: total surface of the GUVs and best fitting obtained with straight lines. Panels D: surfaces A_1 (open green circles) and A_2 (closed green circles) of the spherical caps with radius R_1 and R_2 in the presence of 0.20 mM RL and best fitting obtained with straight lines. Panels E: surfaces A_1 (open blue triangles) and A_2 (closed blue triangles) of the spherical caps with radius R_1 and R_2 in the presence of 0.50 mM RL and best fitting obtained with straight lines. Panel F: volume of GUVs and best fitting obtained with straight lines. (For interpretation of the references to color in this figure legend, the reader is referred to the web version of this article.)

Table 1
Fitting parameters of time-depending geometrical features of GUVs formed by DOPC, SM, CHOL (1:1:1) at different RL concentrations. Parameters $R_i^0, R_i^\infty, t_{0,R_i}$ and Δt_{R_i} (with $i = 1, 2$) regard the sigmoidal approximations (Eq. 4) representing the trend of the radii shown in Fig. 5, panel A. Parameters r_{12}^∞, $t_{0,r_{12}}$ and $\Delta t_{r_{12}}$ regard the sigmoidal curves (Eq. 5) representing the trend of the centre-to-centre distance shown in Fig. 5, panel B. Slopes of the straight lines representing the trend of the total area A, the L_d and L_o areas A_1 and A_2, respectively, and volume V of the GUVs (Fig. 6, panels C-F) are parameters m_A, m_{A_1}, m_{A_2} and m_V, respectively. Corresponding intercepts are $A_0, A_{1,0}, A_{2,0}$ and V_0, respectively. Rates of the fractions of RL molecules interacting with L_d or L_o are γ_d and γ_o (Eqs. S36 and S37 of the SI), respectively.

[RL]	(mM)	0.00	0.20	0.50
R_1^0	(μm)	–	21.88 ± 0.06	14.74 ± 0.03
R_1^∞	(μm)	–	20.49 ± 0.03	14.29 ± 0.02
t_{0,R_1}	(s)	–	527 ± 6	490 ± 10
Δt_{R_1}	(s)	–	50 ± 10	11 ± 9
R_2^0	(μm)	–	21.2 ± 0.1	14.25 ± 0.09
R_2^∞	(μm)	–	19.95 ± 0.06	9.07 ± 0.06
t_{0,R_2}	(s)	–	590 ± 20	491 ± 5
Δt_{R_2}	(s)	–	60 ± 20	60 ± 4
r_{12}^∞	(μm)	–	6.1 ± 0.2	16.3 ± 0.1
$t_{0,r_{12}}$	(s)	–	540 ± 10	499 ± 3
$\Delta t_{r_{12}}$	(s)	–	74 ± 10	96 ± 3
m_A	(10^{-2} μm^2 s^{-1})	0 ± 4	27 ± 4	53 ± 4
A_0	(10^3 μm^2)	3.11 ± 0.03	5.69 ± 0.03	2.63 ± 0.02
m_{A_1}	(10^{-2} μm^2 s^{-1})	–	27 ± 3	50 ± 4
$A_{1,0}$	(10^3 μm^2)	–	3.01 ± 0.02	1.93 ± 0.02
m_{A_2}	(10^{-2} μm^2 s^{-1})	–	0 ± 2	3 ± 1
$A_{2,0}$	(10^3 μm^2)	–	2.67 ± 0.02	0.701 ± 0.007
m_V	(μm^3 s^{-1})	0.0 ± 0.3	0.0 ± 0.6	1.0 ± 0.2
V_0	(10^4 μm^3)	1.79 ± 0.02	4.26 ± 0.04	1.36 ± 0.01
γ_d	(10^{-6} s^{-1})	–	0.10 ± 0.01	0.12 ± 0.01
γ_o	(10^{-6} s^{-1})	–	0.00 ± 0.01	0.023 ± 0.008

parallel to the microscope observation plane, confirming the goodness of the present analysis method. From the other hand, it is worth to notice that the main contribution to the increase of A derives from A_1, revealing that the most important effect of 0.2 mM RL in the plasma membrane mimetic is its insertion in the L_d phase.

A remarkable result was observed by increasing the RL amount to 0.5 mM. During the RL:membrane interaction, the original GUV practically maintains its radius ($R_1^0 \approx R_1^\infty \approx 14$ μm, Fig. 6, panel A, open triangles, and Table 1) whereas the protuded membrane presents a decreasing in size over time (R_2 decreases from ≈ 14 μm to ≈ 9 μm, Fig. 6, panel A, close triangles, and Table 1). The distance r_{12} between the centres of vesicles extends up to *circa* 16 μm and the mid-time transition is $t_{0,r_{12}} \approx 490$ s in very good agreement with t_{0,R_2}, the mid-time transition of R_2 (Fig. 6, panel B (triangles), Table 1). Such membrane remodelling is accompanied by an important total area increase (Fig. 6, panel C, triangles, and Table 1): the slope m_A is ≈ 0.5 μm^2 s^{-1}, corresponding to a relative variation from 180 to 1000 s in the order of 16%) and much less important volume increase (Fig. 6, panel F, triangles, and Table 1: the slope m_V is ≈ 1 μm^3 s^{-1}, corresponding to a relative variation from 180 to 1000 s in the order of 6%). To note, most of the variation of A is due to the increase of A_1 ($m_{A_1} \approx m_A$ and $m_{A_2} \approx 0$, Table 1), thus confirming that the biosurfactant RL mostly interacts with the L_d phase.

In a interesting matter, the fraction of RL molecules into the outer membrane in regard to the total biosurfactants in solution can be derived from the linear increasing of the surface areas A_1 and A_2 from L_d and L_o domains, as a function of time, according to $f_d = \gamma_d t$ and $f_o = \gamma_o t$, respectively. Details of this derivation are fully described in Sec. S4 of the SI. To note, the constant rates of interaction, γ_d and γ_o, are related to the linear fitting parameters of the surfaces A_1 and A_2 (see Eqs. S36 and S37 of the SI).

By assuming that the area per polar head of the DOPC, SM, CHOL lipids are, respectively, $a_{DOPC} = 64$ Å^2, $a_{SM} = 45$ Å^2, $a_{CHOL} = 27$ Å^2 and that the one of RL, derived by SAXS [39], is $a_{RL} = 200$ Å^2, we have obtained the values of γ_d and γ_o shown in the bottom lines of Table 1. As expected, γ_d is always greater than γ_o and both parameters increase with the RL amount in solution.

Results of this analysis deserve some comments. For example, at 0.2 mM RL, after 180 s of RL:membrane interaction, the fraction of RL in the disordered domain is $f_d = (1.9 \pm 0.2) \cdot 10^{-5}$ and the one in the ordered domain results basically zero, within the experimental error ($f_o = (0.0 \pm 0.2) \cdot 10^{-5}$). After 1000 s, the maximum time under microscope GUV observations, our results show an increase of f_d to $(10 \pm 1) \cdot 10^{-5}$ without significant modification of f_o ($f_o = (0 \pm 1) \cdot 10^{-5}$). This finding demonstrates that RLs at this concentration interact preferentially with liquid disordered domain in the experiment time-course. Note that the partition is relatively low in the membrane in respect to the solution.

Completely different is the landscape at 0.5 mM RL. Indeed, after 180 s from the beginning of the interaction, the two fractions are $f_d = (2.2 \pm 0.2) \cdot 10^{-5}$ and $f_o = (0.4 \pm 0.2) \cdot 10^{-5}$, indicating that a not negligible amount of RL also interacts with the ordered domain. Moreover, after 1000 s, the two fractions increase to $f_d = (12 \pm 1) \cdot 10^{-5}$ and $f_o = (2.3 \pm 0.8) \cdot 10^{-5}$. Interestingly, we also observe some scenarios where Rho-PE molecules can be found in the budding region (fluorescence mode) of the membrane after longer period of RL-GUV contact (Fig. S3 of the SI). This means that the presence of RL in the lipid bilayer may either fluidify the ordered phase or promote a sort of lipid lateral rearrangement thus conducting to a less ordered phase in the budding region.

It is worth remarking that the presence of L_o domain *per se* is not enough for budding process (see results displayed on Fig. 6 from GUVs in the absence of RL (squares)). On the other hand, the RL interaction with the outer lipid bilayer triggers budding at the L_o domain site. Supposing that the rate of RL flip-flop is slow, the budding may be partially driven due to alteration of the membrane local spontaneous curvature. This because an area difference between the two monolayers arises due to RL insertion [34]. A budding process may thus take place because it allows for increasing the outside/inside surface ratio of the two leaflets. In addition, as the L_d phase surface area increased due to preferential RL partition in respect to that of L_o phase, the excess free energy associated to the boundary line between the two phases should increase [34,40]. As membrane response, L_o budding occurs which favors line energy reduction. In fact, the distance r_{12} between the two domains increased, concomitantly with the decrease in R_2 radius (Fig. 5, panels C and D, and Fig. 6, panels A and B), resulting in a decrease of the boundary between L_d and L_o phases. Noticeable, we also observed the progression of $L_d - L_o$ domains separation after long RL-GUV incubation time (Fig. S3 of the SI): a tiny neck joining the two domains took place, which reduced significantly the line energy (practically abolishing).

Budding has also been previously observed on POPC:SM:CHOL GUVs induced by sub-*cmc* concentration of Triton-X in less than 10 s of detergent incubation, followed by membrane fission [41]. Here we did not detect fission produced by RL on the lipid bilayers. More recently it has been shown that Triton-X has the ability to rearrange lateral heterogeneity of POPC:SM:CHOL mixtures with selective solubilisation [42]. We should bear in mind that mono and di-RLs, although amphipathic, are bulkier molecules than Triton-X which must hinder their flip-flop to the inner membrane leaflet. As a consequence, lipid bilayer solubilization is precluded, unlike the effects of others synthetic surfactants that are able to translocate to the inner layer [36–38].

Membrane budding of ordered domain has also been reported for other amphipathic molecules as non-ionic detergents, SDS, lyso-PC [43] and a sort of cell-penetrating peptides on cell membranes [44]. In particular, as revealed here, the molecules' partition is preferentially into the L_d phase-containing outer leaflet (even if initially). Therefore, the RL-induced budding mechanism in the inhomogenous GUVs studied, which display lipid-rafts platforms, seems to be a more general rule driven by lipidic forces. Interestingly, it has been shown that changes in membrane curvature towards budding activate massive endocytosis process independent of specific proteins [45]. Here we have demonstrated that the biosurfactant RL, at concentrations above *cmc*, impacts on plasma membrane models and promotes membrane remodelling towards L_o domain budding. Such mechanism may correlate to the endocytosis activation process reported in cells for other amphipathic compounds [43] as well as it may affect the function of specific biomolecules enrolled in lipid rafts. It is worth remarking that, even though RLs can be considered less toxic than usual synthetic surfactants in terms of membrane disruption and/or pores' formation, they can interfere severely in cell homeostasis through lipid membrane remodelling.

4. Concluding remarks

It is well known that rhamnolipids have been used in a large variety of applications as environment bioremediation, biomedicines, foods and cosmetics [46]. However, the concentration-dependent RLs damage at cellular level is still poorly understood. In the current work, we describe the interaction of RLs with plasma membrane models. Our results clearly evidenced the RL molecules insert in the model membrane with no lytic effect for concentrations ranging from 0.1 mM to 0.5 mM (*cmc* of 0.068 ± 0.005 mM in glucose solution). Nevertheless, they are able to promote membrane remodelling. In the case of POPC GUVs, the insertion of RL molecules with time promotes a gradual increase in GUV area until a maximum value was reached (Fig. 4). The GUV restores its original area by releasing the area excess and lateral tension through the formation of small buds that remain linked to the original membrane. Strikingly, RLs on GUVs composed of DOPC:SM:CHOL,

that display L_o-L_d lateral phase separation as rafts platforms, drive L_o domain budding in a micro-scale. Interestingly, our data analysis gives support to conclude that RLs preferentially partition in the L_d phase (at least initially), as highlighted by the values of A_1 and A_2 as well as by the interaction rates γ_d and γ_o.

Of note, the increase propensity of the membrane to phase separate and vesiculate upon RL action may parallel with protrusions recorded in erythrocytes incubated with di-RL [23]. However, although hemolytic effect has been concomitantly detected [23], no increase in membrane permeability nor membrane rupture/solubilization have been here noticed on model lipid bilayers (GUVs). On the other hand, RL effect might impact significantly the cell signaling by triggering changes in membrane curvature which, by turn, leads to budding mediated by lipids lateral segregation, as observed for some other amphipathic compounds [47]. Ultimately, the alterations promoted by RLs in rafts may have an important effect on di(association) of key proteins thus affecting cell homeostatis, eventually leading to cell death as toxicity side effect.

CRediT authorship contribution statement

Benedetta Come: Investigation. **Maressa Donato**: Investigation. **Lucia Francesca Potenza**: Investigation. **Paolo Mariani**: Conceptualization, Writing - original draft. **Rosangela Itri**: Conceptualization, Writing - original draft, Supervision, Funding acquisition. **Francesco Spinozzi**: Conceptualization, Writing - original draft, Formal analysis, Methodology, Software, Supervision.

Declaration of Competing Interest

The authors declare that they have no known competing financial interests or personal relationships that could have appeared to influence the work reported in this paper.

Acknowledgments

RI is recipient from Conselho Nacional de Pesquisa (CNPq, Brazil) for research fellowship. FS thanks to Fabiola Hazizaj and Samuel Pistosini for their extensive use of ImageJ macros.

Appendix A. Supplementary material

Supplementary data associated with this article can be found, in the online version, at https://doi.org/10.1016/j.jcis.2020.08.027.

References

[1] I.C. Ossai, A. Ahmed, A. Hassan, F.S. Hamid, Remediation of soil and water contaminated with petroleum hydrocarbon: A review, Environ. Technol. Innov. 17 (2020). 100526.
[2] M.W. Lim, E.V. Lau, P.E. Poh, A comprehensive guide of remediation technologies for oil contaminated soil – present works and future directions, Mar. Pollut. Bull. 109 (2016) 14–45.
[3] R. Boopathy, Factors limiting bioremediation technologies, Bioresour. Technol. 74 (1) (2000) 63–67.
[4] F.L. Martínez, N.B. Moraga, N. Romano-Armada, M.F. Yañez-Yazlle, V.B. Rajal, V. Irazusta, Stepwise Strategies for the Bioremediation of Contaminated Soils: From the Microbial Isolation to the Final Application, Springer International Publishing, Cham, 2018, pp. 1–28.
[5] R. Dixit, Wasiullah, D. Malaviya, K. Pandiyan, U. Singh, A. Sahu, R. Shukla, B. Singh, J. Rai, P. Sharma, et al., Bioremediation of heavy metals from soil and aquatic environment: An overview of principles and criteria of fundamental processes, Sustainability 7 (2015) 2189–2212.
[6] F. Md, Biosurfactant: Production and application, Journal of Petroleum & Environmental, Biotechnology 3 (2012) 1–6.
[7] K. Muthusamy, S. Gopalakrishnan, T. Ravi, P. Sivachidambaram, Biosurfactants: Properties, commercial production and application, Curr. Sci. 94 (2008) 736–747.
[8] D.R. Perinelli, D. Vllasaliu, G. Bonacucina, B. Come, S. Pucciarelli, M. Ricciutelli, M. Cespi, R. Itri, F. Spinozzi, G.F. Palmieri, L. Casettari, Rhamnolipids as epithelial permeability enhancers for macromolecular therapeutics, Eur. J. Pharm. Biopharm. 119 (2017) 419–425.
[9] D.E. Otzen, Biosurfactants and surfactants interacting with membranes and proteins: Same but different?, Biochimica et Biophysica Acta (BBA) -, Biomembranes 1859 (2017) 639–649.
[10] S.J. Varjani, V.N. Upasani, Critical review on biosurfactant analysis, purification and characterization using rhamnolipid as a model biosurfactant, Bioresour. Technol. 232 (2017) 389–397.
[11] J.L. Parra, J. Guinea, M.A. Manresa, M. Robert, M.E. Mercadé, F. Comelles, M.P. Bosch, Chemical characterization and physicochemical behavior of biosurfactants, J. Am. Oil Chem. Soc. 66 (1989) 141–145.
[12] M. Bustamante, N. Durán, M.C. Diez, Biosurfactants are useful tools for the bioremediation of contaminated soil: a review, J. Soil Sci. Plant Nutr. 12 (2012) 667–687.
[13] X. Long, G. Zhang, C. Shen, G. Sun, R. Wang, L. Yin, Q. Meng, Application of rhamnolipid as a novel biodemulsifier for destabilizing waste crude oil, Bioresour. Technol. 131 (2013) 1–5.
[14] K. Mędrzycka, E. Hallmann, S. Pastewski, Evaluation of surfactant and biosurfactant mixture usefulness in oil removal from soil, based on physicochemical studies and flushing experiments, Environ. Prot. Eng. 35 (2015) 191–205.
[15] L. Santa Anna, G. Sebastian, E. Menezes, T. Alves, A. Santos, N. Pereira Jr., D. Freire, Production of biosurfactants from Pseudomonas aeruginosa PA 1 isolated in oil environments, Braz. J. Chem. Eng. 19 (2002) 159–166.
[16] G. Soberó-Chávez, F. Lépine, E. Déziel, Production of rhamnolipids by pseudomonas aeruginosa, Appl. Microbiol. Biotechnol. 68 (2005) 718–725.
[17] S. Chong, L. Jiang, H. Shao, C. You, G. Zhang, S. Ding, T. Bian, C. Han, Q. Meng, Targeted killing of myofibroblasts by biosurfactant di-rhamnolipid suggests a therapy against scar formation, Sci. Rep. 6 (2016) 37553.
[18] H.G. Mortensen, J.K. Madsen, K.K. Andersen, T. Vosegaard, G.R. Deen, D.E. Otzen, J.S. Pedersen, Myoglobin and α-lactalbumin form smaller complexes with the biosurfactant rhamnolipid than with sds, Biophys. J . 113 (2017) 2621–2633.
[19] M. Sánchez, F.J. Aranda, M.J. Espuny, A. Marqués, J.A. Teruel, A. Manresa, A. Ortiz, Aggregation behaviour of a dirhamnolipid biosurfactant secreted by pseudomonas aeruginosa in aqueous media, J. Colloid Interface Sci. 307 (2007) 246–253.
[20] M. Sánchez, J.A. Teruel, M.J. Espuny, A. Marqués, F.J. Aranda, A. Manresa, A. Ortiz, Modulation of the physical properties of dielaidoylphosphatidylethanolamine membranes by a dirhamnolipid biosurfactant produced by pseudomonas aeruginosa, Chem. Phys. Lipids 142 (2006) 118–127.
[21] A. Ortiz, J.A. Teruel, M.J. Espuny, A. Marqués, A. Manresa, F.J. Aranda, Effects of dirhamnolipid on the structural properties of phosphatidylcholine membranes, Int. J. Pharmaceutics 325 (2006) 99–107.
[22] M. Sánchez, F.J. Aranda, J.A. Teruel, A. Ortiz, Interaction of a bacterial dirhamnolipid with phosphatidylcholine membranes: a biophysical study, Chem. Phys. Lipids 161 (1) (2009) 51–55.
[23] M. Sánchez, F.J. Aranda, J.A. Teruel, M.J. Espuny, A. Marqués, A. Ángeles Manresa, Ortiz, Permeabilization of biological and artificial membranes by a bacterial dirhamnolipid produced by pseudomonas aeruginosa, J. Colloid Interface Sci. 341 (2010) 240–247.
[24] K. Invally, L.-K. Ju, Biolytic effect of rhamnolipid biosurfactant and dodecyl sulfate against phagotrophic alga ochromonas danica, J. Surfactants Deterg. 20 (2017) 1161–1171.
[25] E. Cammarota, C. Soriani, R. Taub, F. Morgan, J. Sakai, S.L. Veatch, C.E. Bryant, P. Cicuta, Criticality of plasma membrane lipids reflects activation state of macrophage cells, J. Roy. Soc. Interface 17 (2020) 20190803.
[26] K. Simons, E. Ikonen, Functional rafts in cell membranes, Nature 387 (1997) 569–572.
[27] K. Simons, D. Toomre, Lipid rafts and signal transduction, Nat. Rev. Mol. Cell Biol. 1 (2000) 31–39.
[28] E. Sezgin, I. Levental, S. Mayor, C. Eggeling, The mystery of membrane organization: composition, regulation and roles of lipid rafts, Nat. Rev. Mol. Cell Biol. 18 (2017) 361–374.
[29] S.L. Veatch, S.L. Keller, Seeing spots: Complex phase behavior in simple membranes, Biochimica et Biophysica Acta (BBA) - Molecular, Cell Res. 1746 (2005) 172–185.
[30] A.G. Ayuyan, F.S. Cohen, Lipid peroxides promote large rafts: effects of excitation of probes in fluorescence microscopy and electrochemical reactions during vesicle formation, Biophys. J. 91 (2006) 2172–2183.
[31] N.F. Morales-Penningston, J. Wu, E.R. Farkas, S.L. Goh, T.M. Konyakhina, J.Y. Zheng, W.W. Webb, G.W. Feigenson, Guv preparation and imaging: Minimizing artifacts, BBA - Biomembranes 1798 (2010) 1324–1332.
[32] C.A. Schneider, W.S. Rasband, K.W. Eliceiri, Nih image to imagej: 25 years of image analysis, Nat. Methods 9 (2012) 671–675.
[33] M. Yanagisawa, M. Imai, T. Masui, S. Komura, T. Ohta, Growth dynamics of domains in ternary fluid vesicles, Biophys. J . 92 (2007) 115–125.
[34] R. Lipowsky, Domains and rafts in membranes - hidden dimensions of selforganization, J. Biol. Phys. 28 (2002) 195–210.
[35] B.K. Yoon, J.A. Jackman, M.C. Kim, N.-J. Cho, Spectrum of membrane morphological responses to antibacterial fatty acids and related surfactants, Langmuir 31 (2015) 10223–10232.
[36] T.P. Sudbrack, N.L. Archilha, R. Itri, K.A. Riske, Observing the solubilization of lipid bilayers by detergents with optical microscopy of guvs, J. Phys. Chem. B 115 (2011) 269–277.

[37] B. Mattei, R.B. Lira, K.R. Perez, K.A. Riske, Membrane permeabilization induced by triton x–100: The role of membrane phase state and edge tension, Chem. Phys. Lipids 202 (2017) 28–37.
[38] P.A. Dalgarno, J. Juan-Colás, G.J. Hedley, L. Piñeiro, M. Novo, C. Perez-Gonzalez, I.D.W. Samuel, M.C. Leake, S. Johnson, W. Al-Soufi, J.C. Penedo, S.D. Quinn, Unveiling the multi-step solubilization mechanism of sub-micron size vesicles by detergents, Sci. Rep. 9 (2019) 12897.
[39] B. Come, R. Itri, P. Mariani, F. Spinozzi, (in preparation).
[40] P.I. Kuzmin, S.A. Akimov, Y.A. Chizmadzhev, J. Zimmerberg, F.S. Cohen, Line tension and interaction energies of membrane rafts calculated from lipid splay and tilt, Biophys. J . 88 (2005) 1120–1133.
[41] G. Staneva, M. Seigneuret, K. Koumanov, G. Trugnan, M.I. Angelova, Detergents induce raft-like domains budding and fission from giant unilamellar heterogeneous vesicles: A direct microscopy observation, Chem. Phys. Lipids 136 (2005) 55–66.
[42] A.C. Caritá, B. Mattei, C.C. Domingues, E. de Paula, K.A. Riske, Effect of triton x–100 on raft-like lipid mixtures: Phase separation and selective solubilization, Langmuir 33 (2017) 7312–7321.
[43] D.W. Hilgemann, M. Fine, Mechanistic analysis of massive endocytosis in relation to functionally defined surface membrane domains, J. Gen. Physiol. 137 (2011) 155–172.
[44] O. Maniti, H.-R. Piao, J. Ayala-Sanmartin, Basic cell penetrating peptides induce plasma membrane positive curvature, lipid domain separation and protein redistribution, Int. J. Biochem. Cell Biol. 50 (2014) 73–81.
[45] M. Fine, M.C. Llaguno, V. Lariccia, M.-J. Lin, A. Yaradanakul, D.W. Hilgemann, Massive endocytosis driven by lipidic forces originating in the outer plasmalemmal monolayer: a new approach to membrane recycling and lipid domains, J. Gen. Physiol. 137 (2011) 137–154.
[46] A.M. Abdel-Mawgoud, F. Lépine, E. Déziel, Rhamnolipids: diversity of structures, microbial origins and roles, Appl. Microbiol. Biotechnol. (2010) 1323–1336.
[47] D.W. Hilgemann, G. Dai, A. Collins, V. Lariccia, S. Magi, C. Deisl, M. Fine, Lipid signaling to membrane proteins: From second messengers to membrane domains and adapter-free endocytosis, J. Gen. Physiol. 150 (2018) 211–224.